Received 1 February 2023; revised 3 May 2023; accepted 20 June 2023.
Date of publication 23 June 2023; date of current version 3 July 2023.

Digital Object Identifier 10.1109/OJUFFC.2023.3289169

Electrode Design Based on Strain Mode Shapes for Configurable PMUTs

AMIRFEREYDOON MANSOORI (Student Member, IEEE), LARS HOFF (Member, IEEE), HAMED SALMANI, AND EINAR HALVORSEN (Member, IEEE)

Department of Microsystems, University of South-Eastern Norway, 3184 Borre, Norway

CORRESPONDING AUTHOR: A. MANSOORI (amirfereydoon.mansoori@usn.no)

This work was supported by the Research Council of Norway under Grant 273248 and Grant 237887.

ABSTRACT Piezoelectric micromachined ultrasonic transducers (PMUTs) with multiple electrodes can be utilized as multi-frequency transducers by exciting selected vibration modes of the diaphragm providing configurability that may be beneficial in modern ultrasound imaging and therapeutic techniques. This requires judicious arrangement of the electrode configuration to excite the desired modes or combination of modes. Optimization of the electrode pattern can be done using full electroacoustic Finite Element Method (FEM) simulations, but this is computationally intensive and gives limited insight into the underlying physics. This paper presents a simple and efficient approach based on the in-vacuum strain mode shapes of the PMUT diaphragm to optimize the electrode configurations for an arbitrary PMUT cell resonating at any flexural mode. Strain mode shapes are obtained both from an analytical model as well as FEM. The proposed method is compared to and verified by full electroacoustic FEM simulations of PMUTs radiating into water. The optimal electrode patterns for the first few flexural modes are found for rectangular PMUTs with three different length-to-width aspect ratios, and examples of configurable PMUTs are given by combining the optimal electrodes at two different modes.

INDEX TERMS Piezoelectric micromachined ultrasonic transducers (PMUTs), dual-frequency transducer, electrode optimization, transducer design.

I. INTRODUCTION

PIEZOELECTRIC micromachined ultrasonic transducers (PMUTs) have emerged as viable alternatives to the conventional bulk piezoelectric technology, in particular for applications where miniaturization, cost, low drive voltages, ease of fabrication and integration to the front-end electronics are of critical importance. Fully-operational PMUT arrays have been reported as intracardiac echo [1] and intravascular ultrasound [2] probes for medical imaging as well as time-of-flight [3] and fingerprint [4] sensors for consumer applications.

However, the use of PMUTs for multi-frequency applications such as harmonic imaging [5], image-guided therapy [6] and ultrasound-mediated drug delivery [7] has been largely limited by its narrow bandwidth, which is attributed to the low electromechanical coupling factor of the PMUT structure. [8] The bandwidth issue can be alleviated at the expense of acoustic power output by constructing an array of cells with different dimensions. When immersed in a high damping fluid such as water, the distinct fundamental vibration modes of the different cells interact and merge into a frequency band with improved bandwidth. Such PMUT arrays have been presented, [9], [10] achieving −6-dB bandwidth of >100%. Furthermore, multiple modes of one PMUT cell can be exploited to enable multi-frequency operation at the cell level. Hajati et al. proposed a dual-frequency PMUT using the first two axisymmetric modes of circular dome-shaped diaphragms [11]. By alternatively using elliptical or rectangular diaphragms, a richer spectrum of vibration modes can be achieved. In addition, the ratio between modal frequencies is tunable through applying a DC bias [12] or varying the lateral aspect ratio [9], [13]. Prior work also demonstrated that merging the first few modes of a diaphragm with a sufficiently large lateral aspect ratio results in a wide frequency band in immersion [13], [14], [15].

One attractive feature of PMUTs is their customization capability via the electrode configuration. This is because the electrode configuration can be readily patterned on the

piezoelectric thin film by lithography. This is the key design factor for effective electromechanical coupling to a given flexural vibration mode of a given PMUT stack. While all of the aforementioned PMUTs utilized a single electrode for operation, a multiple electrode configuration allows for more configurability. The desired individual modes or combination of modes can be effectively excited sequentially or simultaneously where the response of each mode is adjustable through separate electrical ports. There has been only two studies entertaining this idea. Wang and Lee proposed a rectangular PMUT utilizing five top electrodes divided into three sets to individually excite the first three flexural modes. They reported the measured displacement sensitivity in air, but did not consider how this influenced the acoustic performance and did not detail the electrode design procedure [16]. Wu et al. presented a dual-frequency circular PMUT using two ring electrodes optimized by Finite Element Method (FEM) but did not give a systematic electrode design approach [17]. Furthermore, electrodes can be driven differentially by signals of opposite polarity. This was previously shown to enhance the coupling factor and the acoustic power output associated with the fundamental mode [18], [19], but this was not applied to the higher order modes.

Designing configurable multi-mode PMUTs requires the knowledge of the electrode patterns for optimal coupling to the desired vibration modes. This optimization can be performed using full electroacoustic FEM simulations [20], [21] but this is computationally intensive and provides limited insight into the underlying physics. The existing analytical approaches such as energy methods [22], piecewise treatment of the plate equation [23], [24] and Green's function-based solution [25] have mostly focused on clamped circular and annular diaphragms due to simplifications associated with cylindrical symmetry. Electrode optimization were limited to maximizing performance at the fundamental mode considering circular and annular electrodes. Square and rectangular diaphragm PMUTs, however, have been less studied by analytical techniques due to more complex modeling. Horsley at al. developed a model for a clamped square diaphragm based on energy methods and discussed the optimization of an inner square or outer frame-like electrode for operation at fundamental mode [26]. However, the assumed approximate mode shape is applicable neither to higher order modes nor to rectangular diaphragms with other length-to-width ratios. Moreover, the mentioned studies worked with the in-vacuum mode shapes for electrode optimization of PMUTs operating in a fluid medium, but none of them assessed the validity of this approximation.

This paper presents an efficient approach to optimize the electrode configuration for a PMUT cell with arbitrary boundary condition resonating at any flexural mode. By the aid of modal analysis, we first define a modal electrode coupling constant based on the sum of in-plane strain mode shapes of the PMUT diaphragm. For a given PMUT stack, this parameter is directly proportional to the magnitude of the electroacoustic transfer function and will thereby be used as a criterion for optimization of the electrode pattern. The magnitude of the transfer function, defined as the spatially-averaged particle velocity per unit voltage, is chosen to be the measure of PMUT sensitivity. Unlike the center displacement utilized by prior work on multi-mode PMUTs [13], [17], our measure characterizes the transmit sensitivity irrespective of the vibration mode and the diaphragm shape, as it directly translates into the output acoustic pressure. To compute the electrode coupling constant, we start with the product of two beam functions in the longitudinal and transverse directions to approximate the in-vacuum mode shapes of a clamped rectangular diaphragm. This choice of mode shapes is demonstrated to be valid for higher order modes and applicable to a great range of length-to-width ratios. Alternatively, the mode shapes in vacuum were also calculated by FEM. For the sake of comparison in this paper, the FEM modes were also found for clamped rectangular diaphragms. However, FEM mode shapes can in general be obtained with no restriction on boundary conditions or diaphragm shape. Employing both beam functions and FEM mode shapes in vacuum, an electrode coupling constant is obtained for rectangular PMUT diaphragms with different length-to-width ratios resonating at different flexural modes. An extensive design space exploration is performed by varying the geometric parameters of continuous and segmented electrode configurations. This parameter study is repeated for the PMUT operating in water using full electroacoustic FEM simulations and the obtained optimal electrode patterns are compared to those of the proposed method. Finally, we elaborate on the configurability of PMUTs by showing a few examples of how a proper electrode design may be used for multi-frequency operation considering both regular and differential drive schemes.

II. ELECTRODE COUPLING CONSTANT

This section lays out the theoretical foundation of the paper. Fig. 1 shows the schematics of cross-sectional and top views of a typical unimorph PMUT cell. The PMUT diaphragm is mainly composed of a piezoelectric thin film on top of a Si structural layer as shown in Fig. 1(a). The active piezoelectric layer is sandwiched between a grounded bottom electrode and a top electrode configuration, which in general can be described as a plurality of patterned symmetrical electrodes connected to N ports. Fig. 1(b) illustrates that the top electrodes may be continuous or segmented where two or more individual rectangular electroded areas can be interconnected, collectively considered as one port.

The general form of the vibration equation of the PMUT governed by the classical plate theory was previously derived using Hamilton's principle [27] assuming no residual stresses and no applied DC bias to

$$D\nabla^4 w + \rho_0 \frac{\partial w}{\partial t} = \nabla^2 M_p + F_{in}, \tag{1}$$

where w is the out-of-plane displacement, D and ρ_0 are respectively the short-circuit flexural rigidity and mass

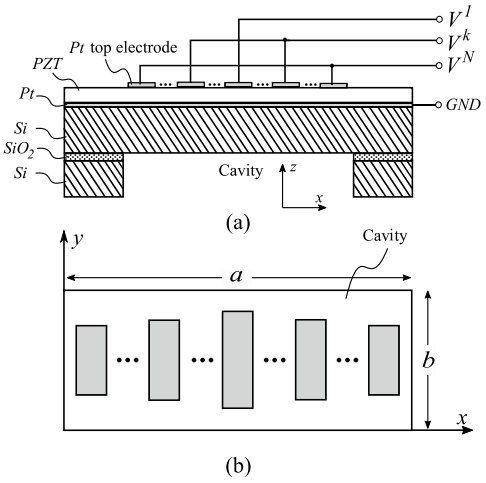

FIGURE 1. Schematic drawings of a unimorph PMUT cell (a) cross-sectional view of the PMUT diaphragm supported by an anchor structure and extended over a cavity. Top electrode configuration is connected to *N* individual ports. (b) top view of the PMUT diaphragm area illustrating the top-electrode layout made of *N* continuous or segmented electrodes on the piezoelectric film.

density of the PMUT. $\nabla^2 M_p$ is the piezoelectric coupling term of the forcing function, and F_{in} is the force from an incoming wave. M_p is the piezoelectrically induced moment resultant arising from the applied voltage across the top electrode configuration associated to the port k and the bottom electrode. Assuming linear piezoelectricity, M_p is obtained by integrating the piezoelectric stress term of the piezoelectric constitutive equations over the thickness of the PMUT and summing over contributions from each electrical port M_p^k [27]. This can be expressed as

$$M_p = \sum_{k=1}^{N} M_p^k = \sum_{k=1}^{N} e_{31,f} \bar{z_p} V^k \Pi^k(x, y), \tag{2}$$

where $e_{31,f}$ is the effective piezoelectric coefficient of the thin film [22], $\bar{z_p}$ is the distance of the mid-plane of the piezoelectric layer from the neutral plane location of the PMUT stack and V^k is the amplitude of the voltage across electrical port k. $\Pi^k(x, y) = 1$ defines the presence of top electrode k at (x, y) while $\Pi^k(x, y) = 0$ defines its absence [27].

Using the modal expansion theorem, the out-of-plane displacement is expressed as a series of mass-normalized two-dimensional mode shapes in vacuum $\phi_i(x, y)$ and modal coordinates $q_i(t)$ as

$$w(x, y, t) = \sum_{i=1}^{\infty} \phi_i(x, y) q_i(t). \tag{3}$$

Under harmonic excitation $v^k(t) = V^k e^{j\omega t}$, the modal displacement response is assumed to take the form $q_i(t) = Q_i e^{j\omega t}$. By following the standard modal analysis procedure, [28] which consists in the substitution of (3) into (1), multiplying by $\phi_l(x, y)$, integration over the surface of the diaphragm and using the orthogonality characteristics of the mode shapes in vacuum, the modal form of the vibration equation in terms of the modal velocity amplitude $U_i = j\omega Q_i$ can be expressed as

$$\left(\frac{\omega_i^2 - \omega^2}{j\omega}\right) U_i = \sum_{k=1}^{N} N_i^k V^k + F_i \tag{4}$$

where ω_i is the natural angular frequency in short circuit condition and F_i is the modal incoming pressure force on the diaphragm for the mode i. The first term on the right hand side of (4) $\sum_{k=1}^{N} N_i^k V^k$ is the modal piezoelectric coupling term of the forcing function resulting from all electrical ports, where N_i^k is the piezoelectric transduction coefficient of the mode i at electrical port k given by

$$N_i^k = e_{31,f} \bar{z_p} B_i^k, \tag{5}$$

and

$$B_i^k = \iint_{A^k} \nabla^2 \phi_i(x, y) dA. \tag{6}$$

The transmitted acoustic power from the PMUT cell driven at electrical port k is related to the electroacoustic transfer function $H^k(\omega)$ associated to electrical port k, defined by

$$H^k(\omega) = \overline{U}(\omega)/V^k(\omega)\Big|_{V^p=0 \quad \text{for} \quad p\neq k}, \tag{7}$$

where ω is the angular frequency and $\overline{U}$ is the spatially-averaged particle velocity over the entire front surface of the diaphragm

$$\overline{U}(\omega) = A^{-1} \iint_{A} \sum_{i=1}^{\infty} U_i \phi_i(x, y) dA. \tag{8}$$

where A is the diaphragm area. This definition effectively accounts for the flexural motion of the PMUT at any given mode. By reciprocity, the same transfer function applies to the receive mode, relating the short-circuit current through electrical port k to the incoming force on the PMUT surface [29]. From (4), (7) and (8), it is evident that the contribution from the mode i to the transfer function H^k is proportional to N_i^k. For a given PMUT stack, the surface integral in (6) computed over the area of top electrode A^k, is the critical parameter for determining $\overline{U}(\omega)$ and we refer to it here as the electrode coupling constant, denoted by B_i^k. This parameter characterizes the interaction between the spatial shape A^k of the top electrode and the flexural vibration of the PMUT. In other words, B_i^k is a measure of how well electrode k is coupled to the mode i. The mechanical interpretation is that, by the classical plate theory, $\nabla^2 \phi_i(x, y)$ is directly proportional to the sum of in-plane strains $S_{xx,i} + S_{yy,i}$, which is henceforth referred to simply as "strain" and thereby

$$B_i^k \propto \iint_{A^k} \left(S_{xx,i} + S_{yy,i}\right) dA. \tag{9}$$

Therefore, considering strain mode shapes makes the electrode design problem more tractable. Strain mode shapes

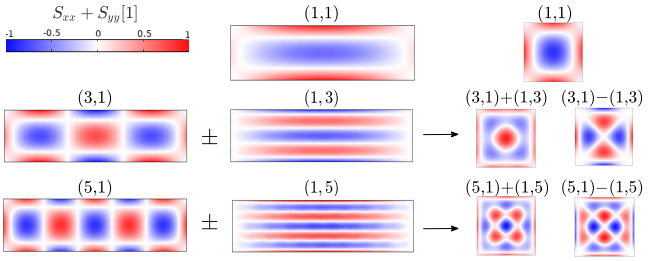

FIGURE 2. Normalized strain mode shapes of different flexural vibration modes of a rather long rectangular PMUT diaphragm ($a/b \gg 1$) versus those of a square PMUT diaphragm ($a/b = 1$). Region of tensile strain are shown in red whereas the compressive strain regions are in blue. Strain nodal zones can be recognized as areas in white.

TABLE 1. Material parameters and layer thicknesses of the PMUT under study.

Parameter	Description	Si	PZT	Pt	Unit
ρ	Density	2320	7750	21450	$[kg/m^3]$
Y	Young's modulus	160	61	168	$[GPa]$
ν	Poisson's ratio	0.22	0.35	0.38	[1]
d_{31}	Piezoelectric coefficient	-	-171	-	$[pC/N]$
ε_{33}^T	Dielectric permittivity	-	1700	-	[1]
t	Thickness	3	1	0.1	$[\mu m]$

of a diaphragm structure typically consist of in-phase and out-of-phase regions, equivalent to regions of tensile and compressive strain, separated by narrow strain nodal zones. This is illustrated in Fig. 2 for the fundamental as well as higher order modes of square and rectangular PMUTs. If the top electrode covers the area of the diaphragm where $S_{xx,i} + S_{yy,i}$ changes sign, the electromechanical response will be diminished as the response from one vibrating area fully or partly cancels that of the area with the opposite phase. To maximize the electromechanical response, the top electrode must cover the diaphragm area of constant phase with respect to strain, away from the nodal zones. A similar discussion was conducted by Erturk et al. for piezoelectric beams for energy harvesting [30], which is extended here for two-dimensional PMUT diaphragms.

III. STRAIN MODE SHAPES

This section provides guidelines for electrode design based on the strain mode shapes in vacuum. Throughout this paper, the proposed PMUT cell has the geometry similar to that of Fig. 1 and the material parameters and thickness of each layer are listed in Table 1. Excluding the anchors, the PMUT diaphragm is approximated as a clamped diaphragm whose width in this study is kept at $b = 55\mu m$ while its length may be varied to study various length-to-width aspect ratios.

To obtain the analytical mode shapes and natural frequencies for short-circuited electrodes, the homogeneous form of (1) needs to be solved. In case of a rectangular diaphragm clamped on four edges, no exact solution appears to be available. However, one approximate solution can be assumed as

TABLE 2. Analytical dimensionless frequencies of the three odd modes of rectangular PMUT with three length-to-width ratios.

a/b	λ_{mn}		
	(1,1)	(3,1)	(5,1)
1	35.11	131.62	308.92
2	24.38	44.40	87.05
4	23.13	28.44	39.40

the product of two beam functions corresponding to the x and y coordinates of the diaphragm [31], which can be expressed as

$$\begin{aligned}\phi_{mn}(x,y) = &\Big[-\cos\alpha_{mn}^x x + \frac{\beta_{mn}^x}{\alpha_{mn}^x}\gamma_{mn}^x \sin\alpha_{mn}^x x \\ &+ \cosh\beta_{mn}^x x - \gamma_{mn}^x \sinh\beta_{mn}^x x\Big] \\ &\times \Big[-\cos\alpha_{mn}^y y + \frac{\beta_{mn}^y}{\alpha_{mn}^y}\gamma_{mn}^y \sin\alpha_{mn}^y y \\ &+ \cosh\beta_{mn}^y y - \gamma_{mn}^y \sinh\beta_{mn}^y y\Big], \end{aligned} \tag{10}$$

where

$$\gamma_{mn}^x = \frac{\cos\alpha_{mn}^x a - \cosh\beta_{mn}^x a}{\frac{\beta_{mn}^x}{\alpha_{mn}^x}\sin\alpha_{mn}^x a - \sinh\beta_{mn}^x a} \tag{11a}$$

$$\gamma_{mn}^y = \frac{\cos\alpha_{mn}^y b - \cosh\beta_{mn}^y b}{\frac{\beta_{mn}^y}{\alpha_{mn}^y}\sin\alpha_{mn}^y b - \sinh\beta_{mn}^y b}. \tag{11b}$$

α_{mn}^x,β_{mn}^x are the boundary condition and mode-dependent eigenvalues associated with the beam function in x and are inter-related to those of the function in y, α_{mn}^y and β_{mn}^y, through the dimensionless frequency of the diaphragm λ_{mn}. The solution procedure to compute all the five parameters is fully described by Xing and Liu [31]. Table 2 lists the dimensionless frequencies of the first three odd modes of PMUTs of three different length-to-width ratios.

Flexural modes of the rectangular PMUT are designated by (m, n), where m and n are the the number of antinodes in longitudinal (x) and transverse (y) directions, respectively. Fig. 2 shows different flexural modes of rectangular PMUTs of different length-to-width aspect ratio. Modes (1,1), (3,1) and (5,1) are the first three odd modes of the rectangular diaphragm in the frequency spectrum.

Modes (3,1) and (5,1) have strain nodal lines parallel to one pair of sides whereas modes (1,3) and (1,5) have strain nodal lines parallel to the other pair of sides. For sufficiently long rectangular diaphragms i.e. $a/b \gg 1$ or $a/b \ll 1$, modes (3,1) and (1,3) resemble beam modes, which are independent in shape and frequency [13]. The same is true for (5,1) and (1,5) modes.

However, as a/b approaches unity, the transverse flexural vibrations become more strongly coupled to the longitudinal vibrations. On account of the symmetry at $a/b = 1$, modes (3,1) and (1,3) compound into the pair of combination modes of (3,1)±(1,3). The plus and minus signs depends

upon whether the component modes vibrate in-phase or out-of-phase together. The (5,1) and (1,5) modes are similarly replaced by the combination modes (5,1)±(1,5). Such modes no longer have nodal lines parallel to the sides. Note that the functions in (10) merely yield the beam modes, these are approximations for the true modes of a rectangular membrane. Modes for the square membrane are reproduced by a linear superposition. It should be noted that here we only consider the odd modes as the even modes have minimal contributions to the electromechanical response due to the cancellation of areas of opposite strain signs. For optimal operation at the fundamental mode having a single strain nodal zone, the top electrode configuration is expected simply to be a single partially-covered continuous electrode as reported in prior work [26], [32], [33]. However, in the case of higher order modes, having multiple strain zones highlights the necessity of exploring segmented configurations.

To verify the proposed analytical mode shape, FEM eigenmode analysis in vacuum was conducted utilizing COMSOL Multiphysics v5.6 (COMSOL AB, Stockholm, Sweden). Fig. 3 compares the strain mode shapes along the two centerlines of the diaphragm, obtained by FEM and the beam functions in (10), for three length-to-width aspect ratios. The strain curves derived from the two methods are in good agreement and strain nodes almost coincide with each other.

The strain mode shapes of square modes (1,1), (3,1)+(1,3) and (5,1)+(1,5) are identical in both directions having 2, 4 and 6 nodes, respectively, as shown in Fig. 3(a)-(c). The rectangular modes (1,1), (3,1) and (5,1) similarly have 2,4 and 6 strain nodes along the length direction whereas maintaining 2 nodes along the width direction, as depicted in Fig. 3(d)-(i). Numerical values of node locations in terms of normalized coordinates in Fig. 3 provide first guesses for the electrode design problem in the next section.

By comparing the location of the strain nodes for a given mode, we find that as a/b increases, the first and the last nodes along the width of the diaphragm move slightly toward its center whereas those along the length of the diaphragm move toward the ends. Fig. 4 verifies this behavior over a greater range of aspect ratios while also revealing that the first and the last nodes in both directions gradually settle in a fixed position for large aspect ratios. However, the middle nodes of the higher-order modes show less sensitivity to the a/b variation, except for the abrupt movement due to the mode transition between $a/b = 1$ and $a/b = 2$. This discussion lead to different optimal electrode configurations for rectangular PMUTs of low to intermediate aspect ratios. The consistency between the analytical and FEM results shown in Fig. 4 demonstrates the applicability of beam functions for electrode design problem over a great range of aspect ratios. It is worth to reiterate that the strain mode shapes remain almost unchanged when the PMUT diaphragm is covered with various ratios of the top electrode because the top electrode has minimal contributions to the mechanics of the diaphragm.

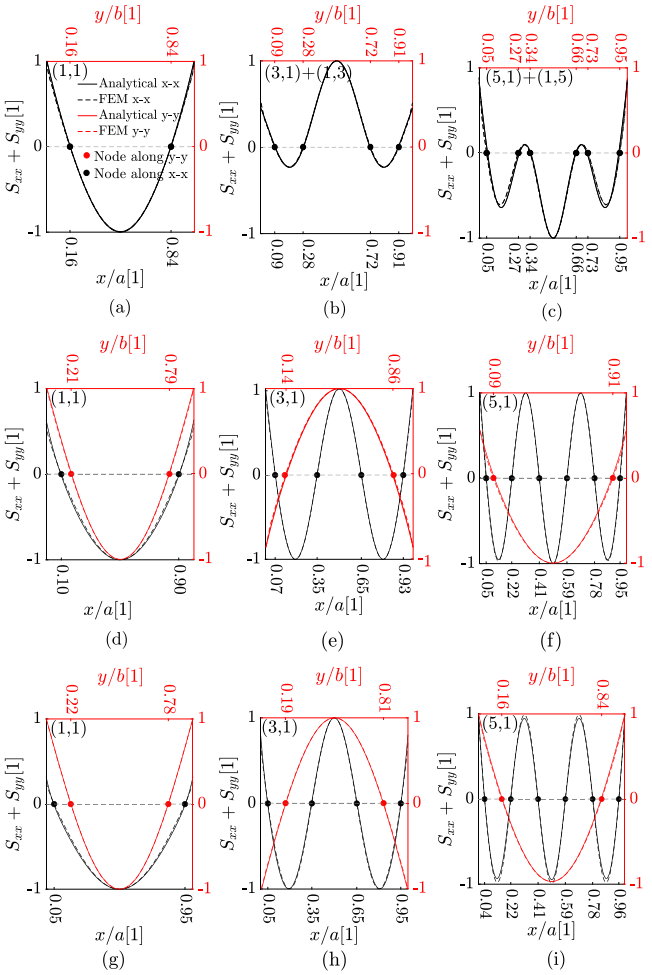

FIGURE 3. Normalized Strain along the diaphragm centerlines in *x* shown in black and in *y* shown in red, obtained by analytical beam functions and FEM eigenmode analysis represented by solid line and dashed line, respectively, corresponding to the three even mode of vibrations for (a)-(c) $a/b = 1$, (d)-(f) $a/b = 2$ and (g)-(i) $a/b = 4$. Strain nodes along the centerlines in x and y are shown by black and red dots, respectively, reported in terms of normalized coordinates. The maximum difference between analytical and FEM strain mode shape amplitudes is 5%.

IV. ANALYSIS OF ELECTRODE CONFIGURATIONS

A. METHODS OF ANALYSIS

The strain mode shapes of Fig. 2 and the estimated intranodal areas from Fig. 3 give a rough idea about the geometry and size of the optimal electrode configuration for maximum performance at a given mode. However, to find accurate optimal parameters, a more rigorous analysis is needed. This was done by comparing results from three different methods:

1) ANALYTICAL COUPLING CONSTANT B_{mn}^k

It involves the computation of the electrode coupling constant B_{mn}^k using the PMUT mode shapes in vacuum, represented by the beam functions in (10). The numerical integration in (6) is performed using MATLAB R2018b (The MathWorks, Natick, MA., USA).

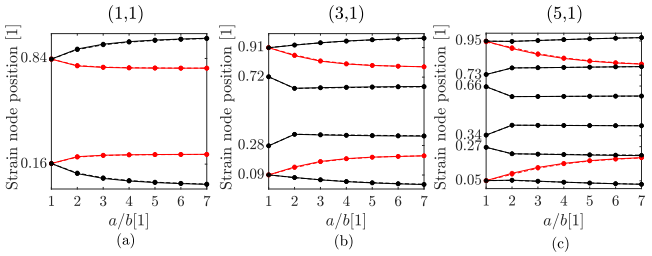

FIGURE 4. **Position of the strain nodes along the diaphragm centerlines in x (in black) and y (in red) versus the length-to-width aspect ratio *a*/*b*: (a) Mode (1,1), (b) Mode (3,1) and (c) Mode (5,1). The maximum difference between analytical and FEM strain node positions is 7%.**

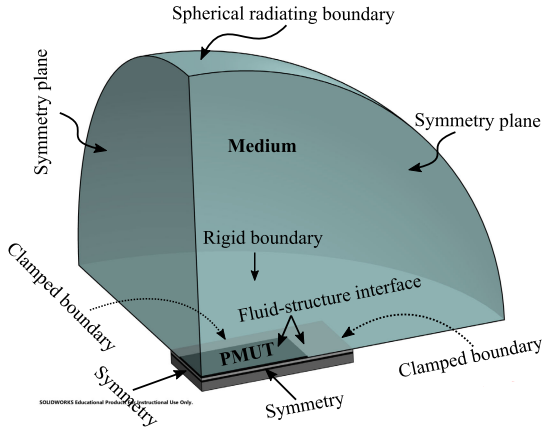

FIGURE 5. **Schematic of the three-dimensional full elecroacoustic FEM setup.**

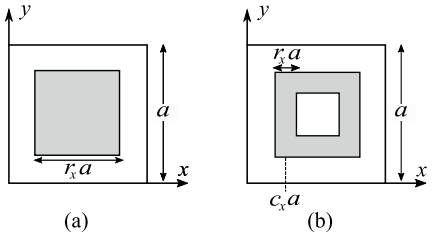

FIGURE 6. **Proposed top electrode configurations for square PMUT: (a) Single continuous (b) Frame-like.**

2) FEM COUPLING CONSTANT B^k_{mn}

This is highly similar to the first method but we choose to work with the equivalent representation of Eq. (6) in Eq. (9) by directly extracting the two-dimensional strain mode shapes from the FEM eigenmode analysis in vacuum and subsequently carrying out a discrete integration using MATLAB. For brevity, we refer to this method as *"FEM coupling constant B^k_{mn}"* since the computed quantity is directly proportional to B^k_{mn}. This method has the advantage of being applicable to any PMUT diaphragm regardless of its shape and boundary condition.

3) FULL ELECTROACOUSTIC FEM

The third approach is to investigate the effect of electrodes on the full electroacoustic performance of the PMUT cell by acquiring the electroacoustic transfer function $H(\omega)$ using FEM in water where the density is $1000 kg/m^3$ and speed of sound is $1500 m/s$. To perform FEM simulations, a three-dimensional model was constructed using COMSOL, as shown in Fig. 5. To minimize computational effort, the PMUT model was reduced to the one-quarter of the diaphragm by imposing the symmetry conditions along the two inner boundaries and clamped conditions along the outer edges. The piezoelectric effect was simulated by coupling the *solid mechanics* and *electrostatics* modules, applying to the PMUT structure. The front surface of the PMUT was exposed to a quarter sphere utilizing the *pressure acoustics* module, which mimics an infinite fluid medium and is interfaced with the electromechanical domain by applying a *fluid-structure interaction* boundary. The rest of the fluid domain surrounding the PMUT cell is defined as the rigid baffle whereas its curved outer surface is set to be a *spherical radiation boundary* $2\lambda_{max}$ away from the diaphragm to eliminate reflections. λ_{max} is the maximum wavelength corresponding to the maximum operating frequency in the propagation medium. Eight elements per λ_{min} in the fluid domain was found sufficient to ensure convergence. λ_{min} is the wavelength at the minimum operating frequency. The electrical boundary condition is applied as AC voltages at the top electrode configuration relative to the bottom electrode as the reference voltage.

B. PMUT WITH $a/b = 1$

Given the symmetry of the square mode shapes, two square electrode configurations of single continuous and frame-like are considered here, as shown in Fig. 6. The single continuous configuration is solely represented by the top electrode side coverage ratio r_x, as illustrated in Fig. 6(a). When r_x was varied within a wide range, analytical and FEM electrode coupling constants computed by the mode shapes in vacuum and the full electroacoustic FEM transfer function followed a similar shape as shown in Fig. 7(a), in agreement with the theory in section II. Fig. 7(a) shows that the continuous electrode couples the most effectively to the mode (1,1) for $r_x = 0.66$ and $r_x = 0.64$, computed through the analytical and FEM electrode coupling constants, respectively. This is in close agreement with the maximum electroacoustic response at $r_x = 0.62$. This optimal coverage almost corresponds to the intranodal area of the single strain zone of mode (1,1), as indicated in Fig. 3(a). This result is also in close agreement with prior work [26]. In the case of the mode (3,1)+(1,3), there are two points of maximum and one point of minimum response as shown in Fig. 7(b). According to the strain mode shapes, the first maximum point corresponds to a small square electrode covering the small strain zone in the center and the second maximum point corresponds to a large square electrode covering both strain zones collectively [see Fig. 2]. This pair of optimal coverage ratios were found to be

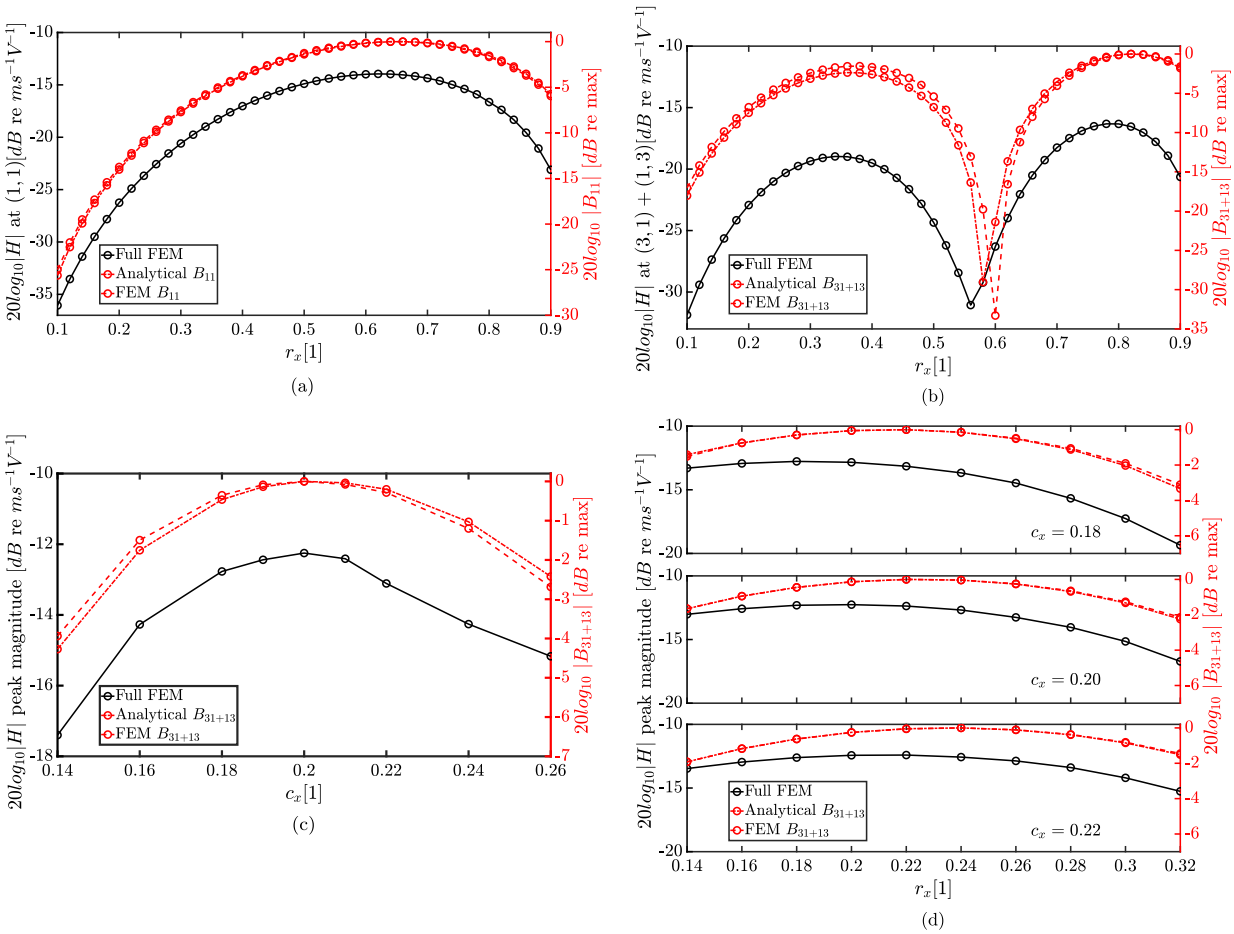

FIGURE 7. Magnitude of the electroacoustic transfer function $|H|$ (in black) compared to the analytical and FEM electrode coupling constants B_{mn} (in red) for a wide range of coverage ratios of a single continuous electrode at (a) mode (1,1), (b) mode (3,1)+(1,3) of a square PMUT. $|H|$ (in black) and Bmn (in red) at mode (3,1)+(1,3) of a square PMUT with a frame-like electrode (c) computed at 9 different locations of midpoint c_x. Every point is reported at their optimum with respect to r_x and (d) computed for a range of coverage ratios r_x at the optimum c_x and the two nearest neighbour locations with a step of 0.02. The dimensionless electrode coverage was also varied with a step of 0.02 in all cases.

(0.36, 0.82), (0.38, 0.82) and (0.36, 0.78) by the analytical and FEM coupling constants and full electroacoustic FEM methods, respectively. The point of minimum response also corresponds to the electrode entirely covering the first strain zone while its edges coincide with the strain anti nodal region of the adjacent zone, so that the response is diminished due to cancellation.

A square frame-like configuration is also contemplated for the effective coupling to the mode (3,1)+(1,3). Fig. 6(b) shows that this configuration is defined by the coverage ratio r_x and the midpoint c_x, representing the distance and the mid location between the inner and outer edges of the frame, respectively. To find the optimal configuration, the coverage ratio was varied while midpoint c_x had been fixed at one location. This was repeated for 9 different locations for c_x and optimal coverage ratio corresponding to each midpoint was evaluated. Fig. 7(c) reveals that the frame midpoint located at 0.20 results in the most effective coupling to the mode (3,1)+(1,3), similarly reported by all the three methods. The coverage ratio at which the electroacoustic response is maximized was found to be 0.20 by full FEM simulations, which agrees well with 0.22 coverage ratio obtained by the other two methods. This can be seen in Fig. 7(d), where the coupling constants and the transfer function magnitude are compared for a range of coverage ratios at the optimum midpoint location and the two nearest neighbour points. The obtained optimal electrode fits well to the frame-like zone of the strain mode shape having an anti nodal region located roughly at 0.19 [see Fig. 3(b)], in close agreement with the obtained optimal parameters.

C. PMUT WITH $a/b > 1$

In the case of rectangular PMUT, a single continuous electrode is defined in terms of the side coverage ratios in both directions, namely r_x and r_y as indicated in Fig. 8(a). Applying the three methods of analysis to a PMUT cell with $a/b = 2$ resulted in the two-dimensional maps of Fig. 9. Every map is a 41 × 41 grid of points as r_x and r_y were varied from 0.1 to 0.9 with a step of 0.02. The electrode coupling constants required significantly less computational effort than the full electroacoustic FEM simulations. For instance, the computation time to obtain the maps of Fig. 9(d) and (e)

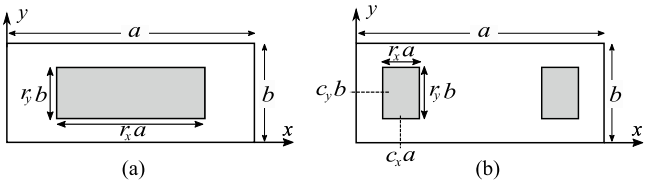

FIGURE 8. Proposed top electrode configurations for rectangular PMUT: (a) single continuous (b) dual-segmented.

TABLE 3. Optimal electrode parameters of single continuous configuration for rectangular PMUTs.

a/b	Mode	Optimal electrode parameters (r_x, r_y)		
		Analytical B_{mn}	FEM B_{mn}	Full FEM
2	(1,1)	(0.78,0.58)	(0.78,0.58)	(0.78,0.56)
	(3,1)	(0.30,0.72) (0.84,0.70)	(0.30,0.72) (0.84,0.68)	(0.30,0.72) (0.84,0.64)
	(5,1)	(0.18,0.80) (0.56,0.80) (0.90,0.78)	(0.18,0.82) (0.56,0.82) (0.90,0.76)	(0.18,0.78) (0.54,0.78) (0.88,0.50)
4	(1,1)	(0.90,0.56)	(0.88,0.56)	(0.88,0.54)
	(3,1)	(0.30,0.62) (0.90,0.60)	(0.30,0.62) (0.90,0.60)	(0.30,0.60) (0.90,0.56)
	(5,1)	(0.18,0.68) (0.56,0.68) (0.92,0.66)	(0.18,0.68) (0.56,0.68) (0.92,0.64)	(0.18,0.64) (0.56,0.62) (0.92,0.60)

was less than one minute compared to roughly 8 hours for generating Fig 9(f) on a an Intel(R) Xeon(R) Gold 6248R CPU running at 3.00 GHz. Fig. 9 shows that the computed analytical and FEM coupling constants exhibit a behavior comparable to what is reported by the full electroacoustic FEM transfer functions for the first three odd modes of the PMUT cell. Similar to the square PMUT, the fundamental mode has a single optimal solution, however the optimal coverage ratio in the longitudinal direction is greater than that in the transverse direction as shown in Fig. 9(a)-(c). The two higher order rectangular modes of (3,1) and (5,1) have 2 and 3 points of maximum coupling as well as 1 and 2 points of minimal coupling, respectively as shown in 9(d)-(i). Again, the points of maximum coupling correspond to the electrodes entirely covering one or multiple strain zones and the points of minimum coupling correspond to the electrodes with edges located at the anti nodal regions leading to the response cancellation. Maps of Fig. 9 also show that the electroacoustic performance is more sensitive to the coverage ratio in the longitudinal direction and this sensitivity becomes more pronounced for higher order modes.

Maps with similar behavior can be generated for $a/b = 4$, however for brevity only the numerical values of the optimal coverage ratios are listed in Table 3 alongside the results for $a/b = 2$. For $a/b = 4$, the most effective coupling to the first three modes occurs at slightly larger coverage ratios in the longitudinal direction and slightly smaller coverage ratios in the transverse direction. This is consistent with the development of strain node locations versus length-to-width ratio shown in Fig. 4.

TABLE 4. Optimal electrode parameters of dual-segmented configuration for rectangular PMUTs.

a/b	Mode	Optimal electrode parameters (c_x, r_x, r_y)		
		Analytical B_{mn}	FEM B_{mn}	Full FEM
2	(3,1)	(0.21,0.28,0.70)	(0.21,0.28,0.70)	(0.21,0.28,0.68)
	(5,1)	(0.14,0.16,0.78) (0.32,0.18,0.82)	(0.14,0.16,0.78) (0.32,0.18,0.82)	(0.14,0.16,0.76) (0.32,0.18,0.80)
4	(3,1)	(0.20,0.30,0.60)	(0.20,0.30,0.60)	(0.20,0.30,0.58)
	(5,1)	(0.13,0.18,0.66) (0.31,0.18,0.68)	(0.13,0.18,0.66) (0.31,0.18,0.68)	(0.13,0.16,0.64) (0.31,0.18,0.68)

The second studied case is a dual-segmented configuration, which is described by the electrode segment center location c_x in addition to its coverage ratios r_x and r_y, as depicted in Fig 8(b). We choose to work with the parameters of the first segment since the second segment is symmetrically located on the other side of the diaphragm.

To obtain the optimal configuration coupled to the higher order modes, the coverage ratios were varied while the center had been fixed at one location. Nine center locations were considered including the strain anti node of modes (3,1) and (5,1), which for the PMUT with $a/b = 2$ are respectively located at 0.21, 0.14 and 0.32 [see Fig. 2(e) and (f)], as well as the two nearest neighbour points with respect to either anti node with a step of 0.02.

Fig. 10(a) compares the full FEM electroacoustic transfer function to the analytical and FEM coupling constants for the selected center locations while the electrode coverage is optimal at each location. The electroacoustic response associated to both modes was found to be maximized when the center of the electrode segment was located at the respective strain anti node. Furthermore, the optimal coverage ratios corresponding to the optimal center locations were found from maps of Fig. 10(b)-(i). The optimal parameters for both cases of $a/b = 2$ and $a/b = 4$ are reported in Table 4. For $a/b = 4$, the optimal center locations are slightly shifted toward the end of the diaphragm and the coverage ratios are almost equal to those of $a/b = 2$ in the longitudinal direction but smaller in the transverse direction, consistent with the strain mode shapes reported in Fig. 3. There is a good agreement between the predictions made by analytical and FEM coupling constants and the full FEM electroacoustic simulations, in terms of both the overall behavior shown in Fig. 10 as well as the numerical values in Table 4.

V. MULTI-FREQUENCY OPERATION

By combining two optimal electrode configuration associated to two modes of vibration, one can enable multi-frequency operation by selectively switching from one configuration to another. For the studied PMUTs, the optimal electrode parameters can be selected from the results in the previous section. The possible arrangements are numerous, therefore

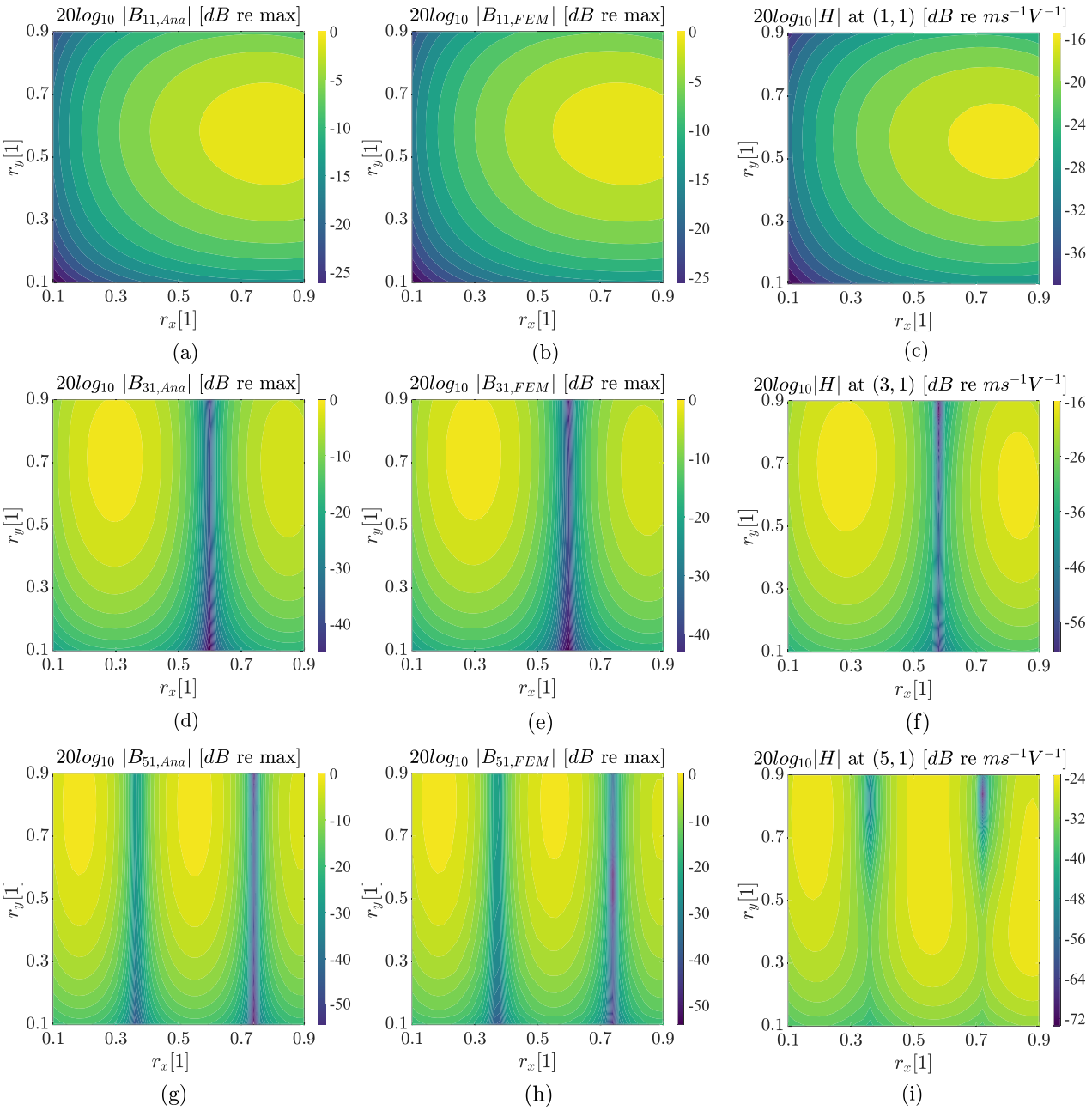

FIGURE 9. Magnitude of the electroacoustic transfer function $|H|$ compared to the analytical and FEM electrode coupling constants B_{mn} for a wide range of coverage ratios of a single continuous electrode at (a)-(c) mode (1,1), (d)-(f) mode (3,1) and (g)-(i) mode (5,1) of a rectangular PMUT with $a/b = 2$. The dimensionless electrode coverage was varied with a step of 0.02 in both directions.

we restrict our attention only to a few simple cases, which are shown in Fig. 11. All arrangements have three sets of electrodes that can be driven through four different schemes as summarized in Table 5. Combining the optimal continuous electrode of the mode (1,1) and the optimal frame-like electrode of the mode (3,1)+(1,3) and making appropriate isolation gaps separating the electrodes results in the arrangement illustrated in Fig. 11(a). The center continuous electrode, middle and outer frame-like electrodes are denoted respectively by I, II and III. The low frequency (LF) port is made up of electrode I combined with electrode II while the high frequency (HF) port consists of electrodes II and III, collectively. Fig. 12(a) shows the simulated electroacoustic transfer functions when LF and HF ports were individually driven by $+1V$. The LF band was centered around 8.3-MHz with a -3-dB fractional bandwidth of 23% while the HF band was centered around 33.7-MHz with a -3-dB fractional bandwidth of 11%.

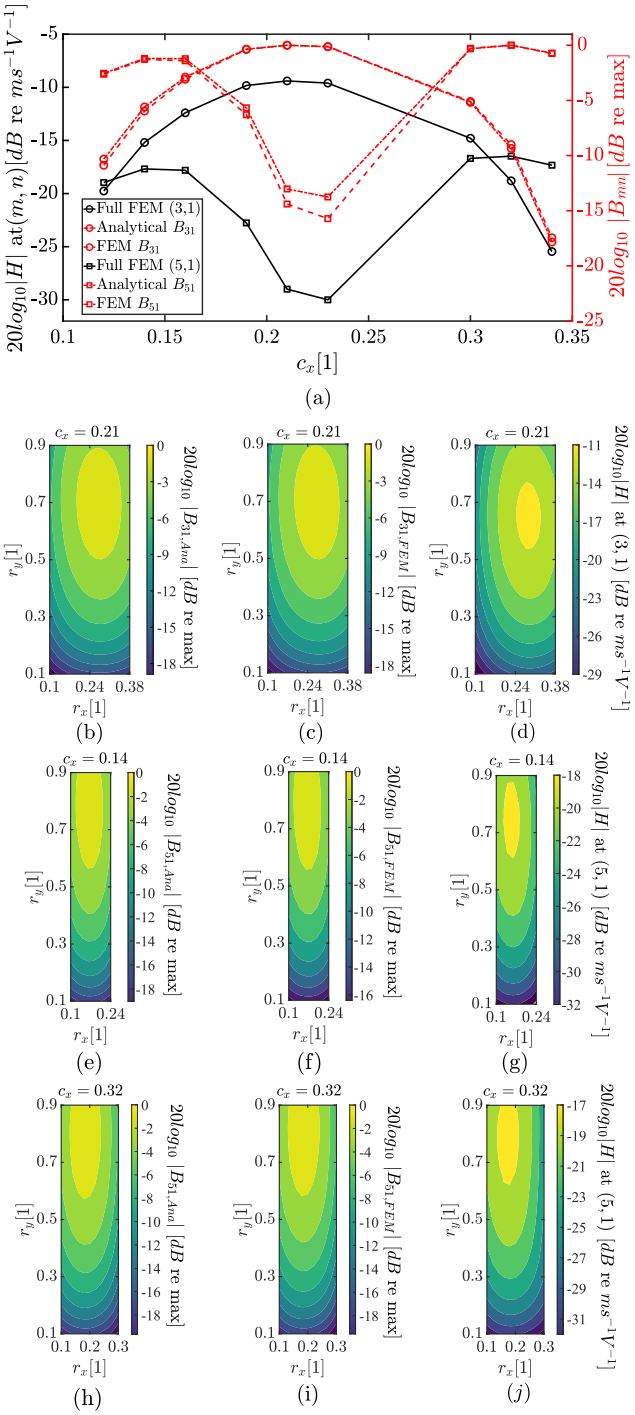

FIGURE 10. Magnitude of the electroacoustic transfer function $|H|$ compared to the analytical and FEM electrode coupling constants B_{mn} at modes (3,1) and (5,1) of a rectangular PMUT with $a/b = 2$ (a) computed at 9 different segment center locations of c_x. Every point is reported at their optimum with respect to r_x and r_y and (b)-(j) computed for possible range of coverage ratios r_x and r_y at the optimum center locations c_x and the two nearest neighbour locations with a step of 0.02. The dimensionless electrode coverage was also varied with a step of 0.02.

To improve the sensitivity of the both LF and HF bands, a differential drive can be applied to a pair of ports through

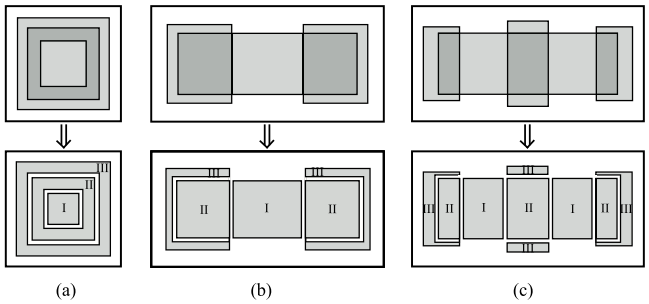

FIGURE 11. Dual-frequency PMUTs with top electrode arrangements made up of combinations of optimal electrodes for (a) modes (1,1) and (3,1)+(1,3) of a PMUT with $a/b = 1$ (b) modes (1,1) and (3,1) of a PMUT with $a/b = 2$ (c) modes (1,1) and (5,1) of a PMUT with $a/b = 2$.

TABLE 5. Different driving schemes for the proposed multi-frequency PMUTs of Fig. 11.

Port(s)	Electrode		
	I	II	III
LF	+1V	+1V	0V
HF	0V	+1V	+1V
LF-differential	+1V	+1V	-1V
HF-differential	-1V	+1V	+1V

input voltage amplitudes of the same magnitude V and opposite polarity denoted using plus(+) and minus(−) signs. This pair must be connected to electrodes covering strain regions of opposite phase. Therefore the pair of LF differential ports consists of electrodes I and II driven by $V^{I+II} = +V$ and the electrode III driven by $V^{III} = -V$, This gives rise to the piezoelectrically-induced strains of opposite signs inside and outside of the strain nodal zone of the mode (1,1), which are proportional to the electrode coupling constants B_{11}^{I+II} and B_{11}^{III} also having opposite signs. Therefore, the electroacoustic response is improved owing to an increase in piezoelectric coupling term of the forcing function:

$$N_{11}^{I+II}V + N_{11}^{(III)}(-V) = e_{31,f}\bar{z}_p V(|B_{11}^{I+II}| + |B_{11}^{III}|) \quad (12)$$

The pair of HF differential port also consists of the electrodes II and III driven by $+V$ and the electrode I driven by $-V$ corresponding to the electrodes on the opposite sides of the strain nodal zone of the mode (3,1)+(1,3). Fig. 12(a) shows almost 2dB and 3.6dB improvements in the LF and HF band sensitivities, respectively, in the case of differential drive by $\pm 1V$ for each individual pair. The larger enhancement in the HF band sensitivity is because $|B_{31+13}^{I}| > |B_{11}^{III}|$. The center frequency and fractional bandwidth for both cases remained almost unchanged.

Fig. 11(b) shows a rectangular PMUT with $a/b = 2$. The optimal continuous electrode of mode (1,1) and the optimal dual-segmented configuration of mode (3,1) [see Table 3 and 4] are combined to enable effective dual-frequency operation. The four driving schemes consistent with the Table 5 were similarly applied to this case and

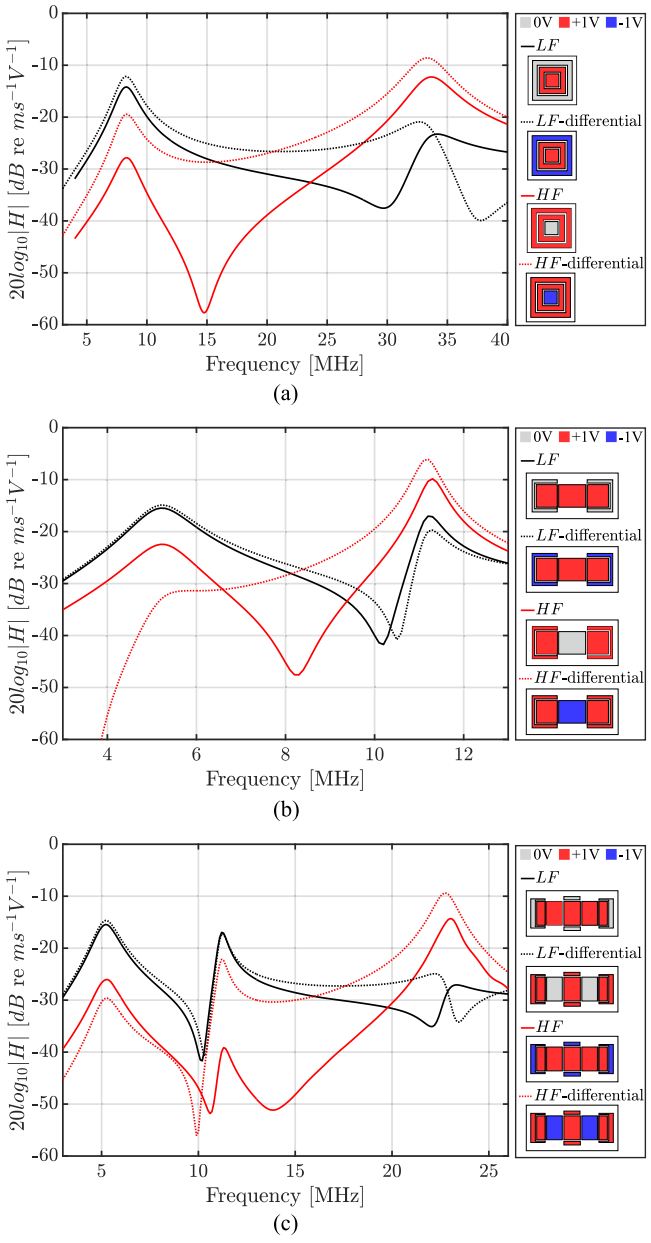

FIGURE 12. full FEM electroacoustic transfer functions of dual-frequency PMUTs (a) with $a/b = 1$ operating at (1,1) and (3,1)+(1,3) modes (b) with $a/b = 2$ operating at modes (1,1) and (3,1) (c) with $a/b = 2$ operating at modes (1,1) and (5,1).

the obtained transfer functions are reported in Fig. 12(b). The LF band was centered around 5.2-MHz with a -3-dB fractional bandwidth of 25% while the HF band was centered around 11.3-MHz with a -3-dB fractional bandwidth of 6%. Improvements through the differential drive are reported to be 0.5dB and 3.7dB for LF and HF bands, respectively. The minor improvement of the LF band is due to the small area and therefore small additional coupling contributed by electrode III.

One may alternatively utilize the first and the third odd modes of the same PMUT diaphragm ($a/b = 2$). In this case, three optimal configurations are combined as shown in Fig. 11(c); the continuous electrode of mode (1,1), the smallest continuous and the dual-segmented configurations of mode (5,1) [see Table 3 and 4]. As shown in Fig. 12(c), the LF band was identical to the previous case while the HF band was moved to be around 23-MHz with a -3-dB fractional bandwidth of 6%. The differential drive boosted the LF band sensitivity by 0.8dB. This rather small increase is explained by the small coupling contributed by the electrode III. Contrary to this, the large area proportional to large coupling of electrode I resulted in 4.9dB enhancement in HF band sensitivity when the PMUT was driven by a HF-differential port. In all above cases, the relative sensitivity of the two bands can be controlled by adjusting the relative magnitude of the input voltage signals [17].

VI. DISCUSSION

The minor deviations between the optimal electrode parameters obtained by the proposed method and the full-FEM simulations may be attributed to integration errors, discretization or fluid loading effects.

Although the proposed method employs the strain mode shapes in vacuum without considering the fluid loading, the predicted optimal electrode parameters for the first few flexural modes are in good agreement with those obtained by the full electroacoustic FEM simulations of a PMUT cell operating in fluid. Therefore, using the mode shapes in vacuum for the calculation of the electrode coupling constant is permitted under the assumption that fluid loading does not change the mode shapes, which was the case for the studied PMUT geometries in this work. This may be violated for larger length-to-width aspect ratios, where mutual acoustic coupling between the closely-spaced resonant modes may modify the mode shapes.

The studied PMUT is a clamped diaphragm with no residual stress. Different boundary conditions and residual stress modify the mode shapes and strain node locations, thus leading to different optimal electrode parameters. Furthermore, the studied electrode geometry was assumed to be made of rectangular areas for simplicity, however rounded electrodes with edges resembling the strain nodal lines would present the true optimal shape.

This article demonstrates that by leveraging PMUT cells as multi-frequency transducers, the designer is rewarded with extensive configurablity in regard to controlling the transfer function. The electrode configuration, input voltage (both magnitude and polarity) and length-to-width aspect ratio may be tuned to yield a great range of desirable characteristics. Switching from one electrode configuration optimized at one vibration mode to another configuration optimized at a different mode allow for multi-frequency operation. One caveat to this solution is that the number of channels in the final PMUT array will increase by a factor of 2 in case of the regular drive and by a factor of 4 in case of the differential drive, which will require more complex on-chip routing.

VII. CONCLUSION

This study has demonstrated how strain mode shapes provide insight into possible optimal electrode configurations for PMUTs. The concept was used to develop an efficient electrode optimization method by defining a modal electrode coupling constant, being proportional to the integral of the strain mode shape in vacuum over the area of the electrode. The method was applied to rectangular PMUTs with length-to-width aspect ratios 1, 2 and 4, and validated against three-dimensional full electroacoustic FEM simulations of the PMUT cell with water loading.

In-vacuum mode shapes were approximated by analytical beam functions, and the resulting optimal electrode geometries were found to agree well with results from full FEM-simulations. FEM eigenmodes in vacuum were tested as an alternative to the analytical beam functions. These results also showed good agreement with the full FEM simulations. When using FEM eigenmodes, the proposed method can be used to identify optimal electrode patterns for any PMUT geometry with arbitrary boundary conditions resonating at any flexural mode.

REFERENCES

[1] D. E. Dausch, K. H. Gilchrist, J. B. Carlson, S. D. Hall, J. B. Castellucci, and O. T. Von Ramm, "In vivo real-time 3-D intracardiac echo using PMUT arrays," *IEEE Trans. Ultrason., Ferroelectr., Freq. Control*, vol. 61, no. 10, pp. 1754–1764, Oct. 2014.

[2] Y. Lu, A. Heidari, and D. A. Horsley, "A high fill-factor annular array of high frequency piezoelectric micromachined ultrasonic transducers," *J. Microelectromech. Syst.*, vol. 24, no. 4, pp. 904–913, Aug. 2015.

[3] R. J. Przybyla et al., "In-air rangefinding with an AlN piezoelectric micromachined ultrasound transducer," *IEEE Sensors J.*, vol. 11, no. 11, pp. 2690–2697, Nov. 2011.

[4] X. Jiang et al., "Monolithic ultrasound fingerprint sensor," *Microsyst. Nanoeng.*, vol. 3, no. 1, pp. 1–8, Nov. 2017.

[5] M. A. Averkiou, D. N. Roundhill, and J. E. Powers, "A new imaging technique based on the nonlinear properties of tissues," in *Proc. IEEE Ultrason. Symp. Int. Symp.*, vol. 2, Oct. 1997, pp. 1561–1566.

[6] D. N. Stephens, D. E. Kruse, A. S. Ergun, S. Barnes, X. M. Lu, and K. W. Ferrara, "Efficient array design for sonotherapy," *Phys. Med. Biol.*, vol. 53, no. 14, pp. 3943–3969, Jul. 2008.

[7] K. K. Andersen, A. Healey, N. L. Bush, M. E. Frijlink, and L. Hoff, "A harmonic dual-frequency transducer for acoustic cluster therapy," *Ultrasound Med. Biol.*, vol. 45, no. 9, pp. 2381–2390, Sep. 2019.

[8] P. Muralt and J. Baborowski, "Micromachined ultrasonic transducers and acoustic sensors based on piezoelectric thin films," *J. Electroceram.*, vol. 12, nos. 1–2, pp. 101–108, Jan. 2004.

[9] A. Hajati et al., "Monolithic ultrasonic integrated circuits based on micromachined semi-ellipsoidal piezoelectric domes," *Appl. Phys. Lett.*, vol. 103, no. 20, Nov. 2013, Art. no. 202906.

[10] C. Nistorica, D. Latev, T. Sano, L. Xu, and D. Imai, "High frequency piezoelectric micromachined transducers with wide bandwidth and high sensitivity," in *Proc. IEEE Int. Ultrason. Symp. (IUS)*, Oct. 2019, pp. 1088–1091.

[11] A. Hajati et al., "Three-dimensional micro electromechanical system piezoelectric ultrasound transducer," *Appl. Phys. Lett.*, vol. 101, no. 25, Dec. 2012, Art. no. 253101.

[12] Y. Kusano et al., "Effects of DC bias tuning on air-coupled PZT piezoelectric micromachined ultrasonic transducers," *J. Microelectromech. Syst.*, vol. 27, no. 2, pp. 296–304, Apr. 2018.

[13] C. Sun, Q. Shi, M. S. Yazici, T. Kobayashi, Y. Liu, and C. Lee, "Investigation of broadband characteristics of multi-frequency piezoelectric micromachined ultrasonic transducer (MF-pMUT)," *IEEE Sensors J.*, vol. 19, no. 3, pp. 860–867, Feb. 2019.

[14] T. Wang, T. Kobayashi, and C. Lee, "Micromachined piezoelectric ultrasonic transducer with ultra-wide frequency bandwidth," *Appl. Phys. Lett.*, vol. 106, no. 1, Jan. 2015, Art. no. 013501.

[15] Q. Shi, T. Wang, T. Kobayashi, and C. Lee, "Investigation of geometric design in piezoelectric microelectromechanical systems diaphragms for ultrasonic energy harvesting," *Appl. Phys. Lett.*, vol. 108, no. 19, May 2016, Art. no. 193902.

[16] T. Wang and C. Lee, "Electrically switchable multi-frequency piezoelectric micromachined ultrasonic transducer (pMUT)," in *Proc. IEEE 29th Int. Conf. Micro Electro Mech. Syst. (MEMS)*, Jan. 2016, pp. 1106–1109.

[17] L. Wu, X. Chen, G. Wang, and Q. Zhou, "Dual-frequency piezoelectric micromachined ultrasonic transducers," *Appl. Phys. Lett.*, vol. 115, no. 2, Jul. 2019, Art. no. 023501.

[18] S. Akhbari, F. Sammoura, B. Eovino, C. Yang, and L. Lin, "Bimorph piezoelectric micromachined ultrasonic transducers," *J. Microelectromech. Syst.*, vol. 25, no. 2, pp. 326–336, Apr. 2016.

[19] Y. Lu, Q. Wang, and D. A. Horsley, "Piezoelectric micromachined ultrasonic transducers with increased coupling coefficient via series transduction," in *Proc. IEEE Int. Ultrason. Symp. (IUS)*, Oct. 2015, pp. 1–4.

[20] F. Akasheh, J. D. Fraser, S. Bose, and A. Bandyopadhyay, "Piezoelectric micromachined ultrasonic transducers: Modeling the influence of structural parameters on device performance," *IEEE Trans. Ultrason., Ferroelectr., Freq. Control*, vol. 52, no. 3, pp. 455–468, Mar. 2005.

[21] S. Sadeghpour, M. Kraft, and R. Puers, "Design and fabrication strategy for an efficient lead zirconate titanate based piezoelectric micromachined ultrasound transducer," *J. Micromech. Microeng.*, vol. 29, no. 12, Dec. 2019, Art. no. 125002.

[22] P. Muralt et al., "Piezoelectric micromachined ultrasonic transducers based on PZT thin films," *IEEE Trans. Ultrason., Ferroelectr., Freq. Control*, vol. 52, no. 12, pp. 2276–2288, Dec. 2005.

[23] F. Sammoura, K. Smyth, and S.-G. Kim, "Optimizing the electrode size of circular bimorph plates with different boundary conditions for maximum deflection of piezoelectric micromachined ultrasonic transducers," *Ultrasonics*, vol. 53, no. 2, pp. 328–334, Feb. 2013.

[24] T. Xu et al., "An analytical equivalent circuit model for optimization design of a broadband piezoelectric micromachined ultrasonic transducer with an annular diaphragm," *IEEE Trans. Ultrason., Ferroelectr., Freq. Control*, vol. 66, no. 11, pp. 1760–1776, Nov. 2019.

[25] K. Smyth and S. Kim, "Experiment and simulation validated analytical equivalent circuit model for piezoelectric micromachined ultrasonic transducers," *IEEE Trans. Ultrason., Ferroelectr., Freq. Control*, vol. 62, no. 4, pp. 744–765, Apr. 2015.

[26] D. Horsley, Y. Lu, and O. Rozen, "Flexural piezoelectric resonators," in *Piezoelectric MEMS Resonators*. Cham, Switzerland: Springer, 2017, pp. 153–173.

[27] K. Smyth, S. Bathurst, F. Sammoura, and S. Kim, "Analytic solution for N-electrode actuated piezoelectric disk with application to piezoelectric micromachined ultrasonic transducers," *IEEE Trans. Ultrason., Ferroelectr., Freq. Control*, vol. 60, no. 8, pp. 1756–1767, Aug. 2013.

[28] S. S. Rao, *Vibration of Continuous Systems*, vol. 464. Hoboken, NJ, USA: Wiley, 2007, ch. 6.

[29] B. A. J. Angelsen, *Ultrasound Imaging—Waves, Signals and Signal Processing*, A. S. Emantec, Ed., 1st ed. Trondheim, Norway, 2000, ch. 3, pp. 3.1–3.109.

[30] A. Erturk, P. A. Tarazaga, J. R. Farmer, and D. J. Inman, "Effect of strain nodes and electrode configuration on piezoelectric energy harvesting from cantilevered beams," *J. Vibrat. Acoust.*, vol. 131, no. 1, Feb. 2009, Art. no. 011010.

[31] Y. F. Xing and B. Liu, "New exact solutions for free vibrations of thin orthotropic rectangular plates," *Compos. Struct.*, vol. 89, no. 4, pp. 567–574, Aug. 2009.

[32] H. S. Choi, M. J. Anderson, J. L. Ding, and A. Bandyopadhyay, "A two-dimensional electromechanical composite plate model for piezoelectric micromachined ultrasonic transducers (pMUTs)," *J. Micromech. Microeng.*, vol. 20, no. 1, Jan. 2010, Art. no. 015013.

[33] E. Ledesma, I. Zamora, A. Uranga, and N. Barniol, "Tent-plate AlN PMUT with a piston-like shape under liquid operation," *IEEE Sensors J.*, vol. 20, no. 19, pp. 11128–11137, Oct. 2020.

AMIRFEREYDOON MANSOORI (Student Member, IEEE) received the M.Sc. degree in microsystems from the University of South-Eastern Norway (USN), Horten, Norway, in 2018, where he is currently pursuing the Ph.D. degree in micro and nano systems, with a focus on design and characterization of piezoelectric micromachined ultrasonic transducers (PMUTs). During his graduate studies, he interned with GE Healthcare, Nice, France, working on piezoelectric material characterization, and TDK InvenSense Milan, Italy, in 2019 and 2021, focusing on PMUT design and validation. Since 2022, he has been with InPhase Solutions, Trondheim, Norway. His research interests include the modeling, design and characterization of ultrasonic transducers and piezoelectric MEMS devices.

LARS HOFF (Member, IEEE) received the M.Sc. degree in physics from the Norwegian Institute of Technology (NTH), Trondheim, Norway, in 1989, and the Ph.D. degree in acoustics from the Norwegian University of Science and Technology (NTNU), Trondheim, in 2000. In 1990, he worked on contrast agents for medical ultrasound imaging with Nycomed Imaging AS, Oslo, Norway, later with NTNU. In 2003, he was with Vestfold University College, Horten, Norway, currently merged into the University South-Eastern Norway, where he was appointed as a Professor in 2008. Since 2015, his main research has been directing toward the Centre for Innovative Ultrasound Solutions (CIUS), where he is currently the Leader of the Work Package Transducers and Electronics. His research interests include acoustics, ultrasound technology, and medical sensor technology.

HAMED SALMANI received the Ph.D. degree from Tarbiat Modares University, Iran. He started his research on piezoelectric devices with the Sharif University of Technology, Iran, in 2011, as a M.Sc. student. Then, he joined the Micro- and Nanoelectromechanical Systems Group, University of South-Eastern Norway (USN), as a Postdoctoral Research Fellow, from 2019 to 2021, where he is currently an Associate Professor. His research interests include analytical and numerical modeling and the characterization of piezoelectric devices, including actuator, energy harvester, ultrasonic transducer, and RF acoustic filters.

EINAR HALVORSEN (Member, IEEE) received the Siv.Ing. degree in physical electronics from the Norwegian Institute of Technology (NTH), Trondheim, Norway, in 1991, and the Dr.Ing. degree in physics from the Norwegian University of Science and Technology (NTNU), Trondheim, in 1996. He has worked both in academia and the microelectronics industry. He is currently with the Department of Microsystems, University of South-Eastern Norway, Horten, Norway, where he is also a Professor. His current research interests include the theory, design and modeling of microelectromechanical devices.